Available online at www.sciencedirect.com
SCIENCE DIRECT®
International Journal of Heat and Mass Transfer 47 (2004) 683–698
International Journal of HEAT and MASS TRANSFER
www.elsevier.com/locate/ijhmt

Large eddy simulation of turbulent heat transfer in a rotating two-pass smooth square channel with sharp 180° turns

Akira Murata *, Sadanari Mochizuki

Department of Mechanical Systems Engineering, College of Engineering, Tokyo University of Agriculture and Technology, 2-24-16 Nakacho, Koganei, Tokyo 184-8588, Japan

Received 11 March 2003; received in revised form 4 August 2003

Abstract

Heat transfer in a rotating two-pass square channel with 180° sharp turns was numerically simulated by using the large eddy simulation with a Lagrangian dynamic subgrid-scale model. In the stationary condition, the heat transfer in and after the turn was increased due to the flow impingement, the flow separation and reattachment, and the reversed flow at the second outer corner. In the rotating condition, the high momentum fluid on the upstream pressure side formed one strong vortex in the turn that transported the high momentum and low temperature fluid to the suction surface side where the heat transfer became high.

1. Introduction

The effective cooling of a gas turbine rotor blade is essential because the higher efficiency of the turbine requires a higher inlet gas temperature. Generally, this blade cooling is performed by film cooling at the external surface of the turbine blade and also by internal forced-convection cooling which uses winding flow passages inside the turbine blade. In the internal forced-convection cooling, the real phenomena are very complicated due to external forces: the Coriolis force and the buoyancy force in the centrifugal acceleration field. In addition to these external forces, the disturbances induced by turbulence promoters (ribs) and 180° sharp turns further complicate the phenomena [1].

As for the heat transfer in smooth and/or rib-roughened channels with the 180° sharp turn, several researchers investigated the detailed spatial variation of the local heat transfer in the stationary condition with various techniques: wall temperature measurement by using hundreds of thermocouples [2,3], naphthalene sublimation technique to measure the local mass transfer, which was transformed into heat transfer by using the analogy between heat and mass transfer [4,5], unsteady wall temperature measurement by using temperature-sensitive liquid crystal [6,7], and wall temperature measurement by using infrared thermography [8]. In these studies, the heat transfer variation induced by the 180° sharp turn was captured: the high heat transfer areas were observed in and after the sharp turn. As for the flow field in the stationary condition, the particle image velocimetry technique was applied to the two-pass channel with the 180° sharp turn, and the detailed two-dimensional flow field was measured by Son et al. [9]. For the rotating condition, however, both the flow velocity and wall temperature measurements become very difficult because of the following two reasons: the high centrifugal force preventing the data acquisition system from normal operation in the rotating system and the difficulty in transferring data from the rotating system to the stationary system. Nevertheless, some researchers have performed measurements in the rotating condition by measuring the wall temperature distribution using thermocouples for the smooth [10–12] and rib-roughened [13–15] wall two-pass channels with the 180° sharp turn. Liou et al. [16] performed the flow velocity measurement of a rotating two-pass smooth channel with the 180° sharp turn by using the laser Doppler anemometer in

* Corresponding author. Tel.: +81-42-388-7089; fax: +81-42-385-7204.
E-mail address: murata@mmlab.mech.tuat.ac.jp (A. Murata).

0017-9310/$ - see front matter © 2003 Elsevier Ltd. All rights reserved.
doi:10.1016/j.ijheatmasstransfer.2003.07.022

Nomenclature

$A_{\text{total,nodim}}$ dimensionless total heat transfer area of channel
c_p specific heat, J/(kg K)
C_S Smagorinsky constant
C_θ coefficient of linear component in energy equation ($=A_{\text{total,nodim}}/32$)
D hydraulic diameter (= side length of straight pass cross-section), m
f friction factor ($=\Delta pD/(2\rho U_m^2 L)$)
F_i external force term
h heat transfer coefficient, W/(m^2 K)
j Colburn's j factor ($=Nu_m/(Re_m Pr^{1/3})$)
ℓ length scale ($=0.5D$), m
L total duct-axial length of two-pass channel ($=22D$)
Nu Nusselt number ($=hD/\lambda$)
Δp pressure loss between channel inlet and outlet, Pa
Pr Prandtl number ($=0.71$)
Pr_{SGS} Prandtl number of subgrid-scale model ($=0.5$)
$\dot{q}$ wall heat flux, W/m^2
Re_m Reynolds number based on bulk mean velocity ($=U_m D/\nu$)
Re_* Reynolds number based on friction velocity ($=u_*\ell/\nu$)
Ro_m rotation number based on bulk mean velocity ($=\omega D/U_m$)
Ro_* rotation number based on friction velocity ($=\omega\ell/u_*$)
S_{ij} rate-of-strain tensor
t dimensionless time
T temperature, K
T_{linear} linearly increasing component of temperature, K
T_r friction temperature ($=\dot{q}/(\rho c_p u_*)$), K
u, v, w dimensionless velocities in x, y, z directions
u_* mean friction velocity calculated from mean pressure gradient in x direction, m/s
$u_{*\text{mod}}$ mean friction velocity estimated by using bulk mean velocity, m/s
$\bar{u}_m$ dimensionless bulk mean velocity in x direction calculated at the entrance $\left(=\frac{1}{4}\int_{-1}^{1}\int_{-1}^{1}\bar{u}\,dy\,dz\right)$
U_m bulk mean velocity, m/s
x, y, z dimensionless Cartesian coordinates
$\alpha_{SGS\,j}$ subgrid-scale energy flux
$\Delta_1, \Delta_2, \Delta_3$ grid spacing in ξ, η, ζ: directions expressed in (x, y, z) coordinates' scale
λ thermal conductivity, W/(m K)
ν kinematic viscosity, m^2/s
ν_{SGS} dimensionless subgrid-scale eddy viscosity
ω angular velocity, rad/s
ρ density, kg/m^3
θ dimensionless temperature ($=(T-T_{\text{linear}})/T_r$)
$\tau_{SGS\,ij}$ subgrid-scale stress tensor
$\tau_{w,s}$ streamwise component of wall shear stress, Pa
ξ, η, ζ curvilinear coordinates

Subscripts and superscripts

b bulk value
B Blasius
L local value
m duct average or based on bulk mean velocity
w wall
∞ fully developed
* friction velocity or defined by using u_*
+ dimensionless value based on inner scales
− grid resolvable component

addition to the detailed heat transfer measurement by using the transient liquid crystal method. However, it is very difficult to perform the experiments in the rotating condition which can identify both the flow structure and its influence on the heat transfer at the same time. Thus, further progress in experimental studies has so far been prevented.

In previous numerical studies of the serpentine flow passage with the 180° sharp turn, the Reynolds-averaged Navier–Stokes equation with a turbulence model was adopted: Banhoff et al. [17] used the k–ε two-equation turbulence model and the Reynolds stress equation model with the wall function, and Lin et al. [18] used the low-Reynolds number two-equation turbulence model without the wall function. Although this approach using the Reynolds-averaged turbulence model could reproduce the heat transfer of blade cooling to a certain extent, even the Reynolds stress equation model has empirical constants and functions, and therefore the applicability of the model should carefully be examined. Recent advancement in computers enables us to numerically simulate the fluctuating components of the turbulent flow by using the large eddy simulation (LES) or the direct numerical simulation (DNS), and the techniques were applied to the smooth straight duct in the stationary [19–21] and rotating [22,23] conditions. Because LES and DNS directly resolve temporal variation of the fluctuating components, the results are more

universal, in other words, more free from the empirical modeling than the Reynolds-averaged turbulence models. Although LES also has empirical constants and functions, the modeling of the turbulence is confined to the subgrid-scale turbulence, and therefore the effect of the empirical modeling on the result is ideally less than that in the Reynolds stress equation model. Recently, the authors performed the numerical analyses by using a dynamic subgrid-scale model for a rotating angled-rib-roughened straight duct using a coordinate system fitted to the angled ribs [24,25]. However, the effect of the 180° sharp turn on the fluid flow and heat transfer has not been discussed yet, because solving the whole two-pass channel with the sharp turn requires the huge computational domain and therefore the unacceptably high computational load.

This study examines how the 180° sharp turn affects the heat transfer and also the effect of the interaction between the sharp turn induced and the Coriolis induced secondary flows on the heat transfer. The large eddy simulation of a very large computational domain was made possible by adopting the parallel computing technique, and it was performed on a supercomputer of massive parallel processors for both stationary and rotating conditions.

2. Numerical analysis

Fig. 1 shows the computational domain and coordinate system used in this study. The duct had a square cross-section with a side length of D. The coordinate system was fixed to a rotating channel that had an angular velocity of ω with respect to the axis of rotation parallel to the x-axis. The axial direction of the channel straight pass was chosen in the z direction; the x and y directions were the parallel and perpendicular direction to leading/trailing walls, respectively. In this study, the side walls referred to the leading and trailing walls whether the channel rotated or not. The inner and outer walls at the turn A was called the inner and outer walls, respectively. Therefore, it should be noted that "the inner wall" and "the outer wall" of this study came to the outer and inner sides at the turn B, respectively, although the discussion of this study was for the turn A unless otherwise explained. The present procedure of the numerical analysis was the same as our recent studies [24,25] in the generalized curvilinear coordinate system. After applying a filtering operation to the incompressible Navier–Stokes equation with a filter width equal to the grid spacing [21], the dimensionless governing equations scaled by a length scale, ℓ $(= 0.5D)$, and mean friction velocity, u_*, became a set of dimensionless governing equations with respect to grid resolvable components indicated by overbars as $(\bar{u}, \bar{v}, \bar{w})$ under the assumption of constant fluid properties. In order to simulate a fully developed situation, the pressure and temperature fields were decomposed into the steady and x-directional linear component and the remaining component [26]. By this decomposition, the latter component of the pressure and temperature fields can be treated using a periodic boundary condition in the x direction. As shown in Eq. (1), F_i is an external force term including the Coriolis force, and the buoyancy term

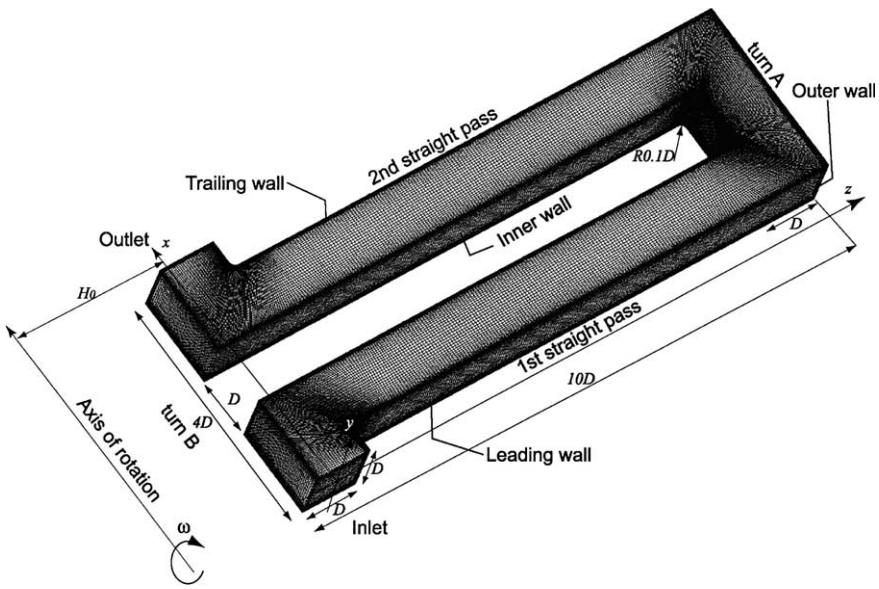

Fig. 1. Schematic of a rotating two-pass smooth square channel with sharp 180° turns.

was ignored in this study. The mean pressure gradient term (with a value of 2) was added to the external force term as follows:

$$F_i = \begin{pmatrix} 2 \\ 2Ro_*\bar{w} \\ -2Ro_*\bar{v} \end{pmatrix}. \tag{1}$$

In this study, the friction velocity, u_*, was calculated from the force balance between the mean pressure gradient in the x direction and the wall shear stress as follows:

$$\rho u_*^2 = \frac{\ell}{2}\left|\frac{\mathrm{d}p}{\mathrm{d}x}\right|_{\mathrm{m,dim}}. \tag{2}$$

Here, the mean pressure gradient with the subscript, "dim", means the value with dimension, and it drives the flow in the x direction. By non-dimensionalizing Eq. (2), the dimensionless mean pressure gradient value of 2 came out. Because the mean pressure gradient which drove the flow in the x direction was set to be constant in this study, the flow rate varied depending on the flow condition (the rotation number); therefore, the flow rate was not known a priori, and it was calculated from the resultant computed flow field after the fully developed condition was attained. In this study, the fully developed condition was judged by the statistical steadiness.

The temperature was made dimensionless by using a linearly increasing component of temperature, T_{linear}, and a friction temperature, T_{r}, as $\theta = (T - T_{\mathrm{linear}})/T_{\mathrm{r}}$. Accordingly, the dimensionless energy equation was derived for the grid resolvable component, $\bar{\theta}$. The governing equations in the Cartesian coordinates (x, y, z) were transformed into generalized curvilinear coordinates (ξ, η, ζ). At the middle of the first straight pass, the ξ, η, and ζ directions coincided with the x, y, and z directions, respectively. The governing equations in the curvilinear coordinate system were expressed as follows [27]:

$$\frac{1}{J}\frac{\partial J\overline{U}^j}{\partial \xi^j} = 0, \tag{3}$$

$$\frac{\partial \bar{u}_i}{\partial t} = -\overline{U}^j\frac{\partial \bar{u}_i}{\partial \xi^j} - \frac{\partial \xi^j}{\partial x_i}\frac{\partial \bar{p}}{\partial \xi^j} + \frac{1}{Re_*}\frac{\partial \xi^j}{\partial x_\ell}\frac{\partial}{\partial \xi^j}\left(\frac{\partial \xi^k}{\partial x_\ell}\frac{\partial \bar{u}_i}{\partial \xi^k}\right) + \frac{\partial \xi^k}{\partial x_j}\frac{\partial \tau_{\mathrm{SGS}\,ij}}{\partial \xi^k} + F_i, \tag{4}$$

$$\frac{\partial \bar{\theta}}{\partial t} = -\overline{U}^j\frac{\partial \bar{\theta}}{\partial \xi^j} - C_\theta\frac{\bar{u}}{\bar{u}_{\mathrm{m}}} + \frac{1}{Re_*Pr}\frac{\partial \xi^j}{\partial x_\ell}\frac{\partial}{\partial \xi^j}\left(\frac{\partial \xi^k}{\partial x_\ell}\frac{\partial \bar{\theta}}{\partial \xi^k}\right) + \frac{\partial \xi^k}{\partial x_j}\frac{\partial \alpha_{\mathrm{SGS}\,j}}{\partial \xi^k}, \tag{5}$$

where $\overline{U}^j$ was a contravariant component of velocity, and the following expressions were assumed: $J = \partial(x, y, z)/\partial(\xi, \eta, \zeta)$, $(x_1, x_2, x_3) = (x, y, z)$, and $(\xi^1, \xi^2, \xi^3) = (\xi, \eta, \zeta)$.

Subgrid-scale components of stress, $\tau_{\mathrm{SGS}\,ij}$, and energy flux, $\alpha_{\mathrm{SGS}\,j}$, were expressed as follows:

$$\tau_{\mathrm{SGS}\,ij} = 2\nu_{\mathrm{SGS}}\overline{S}_{ij}, \tag{6}$$

$$\alpha_{\mathrm{SGS}\,j} = \frac{\nu_{\mathrm{SGS}}}{Pr_{\mathrm{SGS}}}\frac{\partial \xi^k}{\partial x_j}\frac{\partial \bar{\theta}}{\partial \xi^k}, \tag{7}$$

where

$$\overline{S}_{ij} = \frac{1}{2}\left(\frac{\partial \xi^k}{\partial x_j}\frac{\partial \bar{u}_i}{\partial \xi^k} + \frac{\partial \xi^k}{\partial x_i}\frac{\partial \bar{u}_j}{\partial \xi^k}\right), \tag{8}$$

$$\nu_{\mathrm{SGS}} = C_{\mathrm{S}}^2(\Delta_1\Delta_2\Delta_3)^{2/3}\sqrt{2\overline{S}_{ij}\overline{S}_{ij}}. \tag{9}$$

Because the flow field of this study has no homogeneous direction, we adopted the Lagrangian dynamic subgrid-scale model of Meneveau et al. [28] which averages the value of C_{S} along the path-line for a certain distance. As for the coefficient of the Lagrangian averaging time scale, the same value of 1.5 as that in [28] was used. The turbulent Prandtl number for the subgrid-scale component, Pr_{SGS}, was set to 0.5 [29]. These values were mainly tested for the two-dimensional channel turbulence, and therefore there is room for further optimization of them to the present complicated flow passage. However, it should be noted that the results in [28] showed acceptably small sensitivity to the coefficient of the Lagrangian averaging time scale, and the value of Pr_{SGS} also showed small sensitivity to the flow types and grid resolution in [29]. The width of the test filter was double the grid spacing.

Discretization was performed by a finite difference method using the collocated grid system [27]. The spatial and temporal discretization schemes were similar to those of Gavrilakis [20]: the second order central differencing method and the Crank–Nicolson method for the viscous term, and the second order differencing method satisfying the conservative property [27] and the second order Adams–Bashforth method for the convective term. The external force term was also treated by the second order Adams–Bashforth method. The pressure field was treated following the MAC method [30]. At the wall boundary, no-slip and constant heat flux conditions were imposed. At the inlet and outlet boundaries, the periodic boundary condition [26] was imposed in order to obtain a fully developed flow. The boundary conditions of the intermediate velocities and the pressure were set following the procedure of [31,32].

The local Nusselt number, Nu_{L}, was calculated from the wall temperature as follows:

$$Nu_{\mathrm{L}} = \frac{2Re_*Pr}{\bar{\theta}_{\mathrm{w}} - \bar{\theta}_{\mathrm{b}}}. \tag{10}$$

The averaged Nusselt number was calculated by using the integrally averaged temperature difference for the area in question.

Table 1
Dimensionless number range of this study and the duct averaged values of f and Nu_m

Re_*	Ro_*	Re_m	Ro_m	f/f_B	Nu_m/Nu_∞ $(= j/j_\infty)$
700	0	4099	0	4.30	1.93
1000	1	4028	0.99	9.04 (+110%)	2.39 (+23.8%)
		(4150)	(0.96)	(8.58 (+100%))	(2.37 (+22.8%))
1500	2	3926	3.06	21.28 (+395%)	2.77 (+43.5%)
		(3921)	(3.06)	(21.33 (+396%))	(2.81 (+45.6%))

The values in the second line are for higher grid resolution of $71\times71\times761$ with reduced sample size of 30,000 steps. The percentage values are the increase as compared to the stationary case.

As explained above, the bulk mean Reynolds number, Re_m, varies depending on the rotation number, Ro_*. In order to extract only the effect of duct rotation on the heat transfer, the value of Re_* $(= u_*\ell/\nu)$ was varied depending on Ro_* $(= \omega\ell/u_*)$ so as to keep the values of Re_m constant. The resultant combinations of (Re_*, Ro_*) were $(700, 0)$, $(1000, 1)$, and $(1500, 2)$. The conversion of the dimensionless numbers of this study (Re_*, Ro_*) defined by the mean friction velocity and the length scale, $0.5D$, into those of (Re_m, Ro_m) defined by the bulk mean velocity and the hydraulic diameter, D, was summarized in Table 1.

As shown in Fig. 1, the structured grid system was generated by using Gridgen Ver. 14 (Pointwise Inc.). The grids in the physical domain were contracted to the walls and the corners. The grid number was mainly $47\times47\times761$ in ξ, η, ζ directions, and this grid configuration gave a grid spacing of $\Delta_1^+ = 0.14$–17.3, $\Delta_2^+ = 0.15$–12.6, and $\Delta_3^+ = 1.5$–16.4. Here, the inner length scale of $\nu/u_{*\mathrm{mod}}$ was used, because the friction velocity, u_*, defined in Eq. (2) overestimated the value. In Eq. (2), the streamwise direction was assumed to be only in the x direction, and therefore it cannot account for the longer total flow distance caused by the change of the streamwise direction in the two-pass channel. In order to estimate appropriate inner length and time scales, the friction velocity, $u_{*\mathrm{mod}}$, was calculated by using the resultant flow rate for each condition and the Blasius equation. The effect of the grid spacing on the computed result was checked by increasing the grid number to $71\times71\times761$ for several cases, and no major difference was observed as shown in Table 1. The time step interval was $\Delta t = 1.0\times10^{-4}$, which can be expressed as $\Delta t^+ = 0.014$ when made dimensionless by an inner time scale, $\nu/u_{*\mathrm{mod}}^2$.

In order to deal with the very high computational load of this study, the computational domain was decomposed into 64 sub-domains in the duct-axial (ζ) direction, and the parallel computing technique was applied. Each sub-domain's computation was performed on a different CPU on HITAC SR8000 (Information Technology Center, The University of Tokyo). When the algebraic equation for each variable was solved by using the SOR method, the values at the sub-domain boundaries were transferred to the neighboring sub-domains by using MPI functions in each iteration.

The computation was started using the result of the similar condition as an initial condition. At first, the calculations were carried out till the statistically steady flow condition was attained. After that, additional 120,000 steps ($t = 12$ or $t^+ = 1700$) were performed for computing the statistical values. This total time step was adopted as the sample size large enough to give the steady statistical values after some preliminary computations changing the sample size. This 120,000 step computation needed about 12.8×64CPU hours.

3. Results and discussion

Fig. 2 shows the variation of the transversely averaged Nusselt number in the duct-axial direction. The Nusselt number of this study was normalized using the following empirical correlation for a fully developed pipe flow [33]:

$$Nu_\infty = 0.022 Re_m^{0.8} Pr^{0.5}. \tag{11}$$

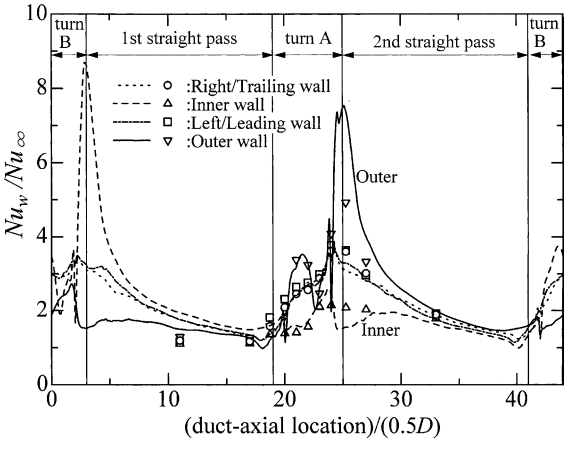

Fig. 2. Transversely averaged Nusselt number variation in the duct-axial direction ($Re_* = 700$, $Re_m = 4099$, $Ro_* = 0$; experimental results (symbols) are from Murata et al. [2] for $Re_m = 5000$).

The symbols in the figure are from the experimental results of Murata et al. [2] for the same sharp turn geometry. In the numerical results, the coincidence of two side-wall values (the leading and trailing walls) confirms the flow symmetry required by the symmetric channel geometry. In the experiment, the fully developed flow entered the test section; therefore, at the first straight pass, the Nusselt numbers of the experiment show no difference on four walls and are lower than the numerical results. At the turn section, the Nusselt number increases. The outer wall gives the highest value, and its variation is also large. In and after the turn A, the agreement between the numerical and experimental results are good, although the numerical result gives the higher value on the outer wall at the turn outlet location as compared to the experimental result.

Fig. 3 shows the stationary results of the local Nusselt number (Fig. 3(a)) and the streamwise component of the wall shear stress (Fig. 3(b)) on all four walls by viewing the flow channel from six different directions. In Fig. 3(b), zero shear stress areas are indicated by a white line. In the calculation of the streamwise component of the wall share stress, the streamwise direction was approximated by the ζ direction. In this stationary case, the numerical results reproduce the symmetric profile with respect to the x–z mid-plane required by the geometric symmetry. In Fig. 3(a), the Nusselt number increases in and after the turn. As was seen in Fig. 2, the outer wall gives two peaks: one is at the middle of the outer end wall and the other is at the second outer corner in the turn followed by the very high Nusselt number on the outer wall extending to the second straight pass. On the contrary, the Nusselt number on the inner wall stays low. On the side walls (the leading and trailing walls in the figure), the high Nusselt number area appears at the turn outlet, and it is shifted to the outer wall. These Nusselt number variations have also been observed in the previous experiments [5–8], and they were explained by the flow impingement onto the outer end wall in the turn and onto the outer wall after exiting the turn using the two-dimensional velocity field [9]. The flow impingement is confirmed by the high shear stress region in Fig. 3(b) on the outer end wall in the turn and on the outer wall after the turn. The low heat transfer on the inner wall is attributed to the flow separation, and it is also confirmed by the negative shear stress on the inner wall in and after the turn. When the two outer corner regions are examined, both are covered by the negative shear stress and therefore the existence of the flow separation is confirmed. What is interesting is the second outer corner region; though the region is covered by the negative shear stress, it gives the high Nusselt number as seen in Fig. 3(a). In this second outer corner region, the high heat transfer is correlated with the negative wall shear stress, and similar correlation was observed in the rib-roughened duct case at the high heat transfer region in front of the ribs [24,25]. The high heat transfer area correlated with the reverse flow can be understood by the unsteady movement of the high momentum fluid which flows in the reverse direction due to the impingement onto the perpendicular wall (or the rib). At the entrance of the turn, the shear stress on the inner and leading/trailing walls becomes high, but this region does not show the high heat transfer because it is covered by the high temperature fluid.

The results of the rotating cases ($Ro_* = 1$ and 2) are shown in Figs. 4 and 5. In this study, the trailing and leading walls of the first straight pass correspond to the pressure and suction surfaces, respectively, and opposite relation holds in the second straight pass. The pressure and suction surfaces are defined with respect to the Coriolis induced secondary flow, which impinges onto the pressure surface. In Fig. 4 of $Ro_* = 1$, the pressure surface shows the higher values both in the Nusselt number and the wall shear stress. In the turn A, the high heat transfer area on the leading wall is extended and intensified, but that on the trailing wall is confined to the second outer corner region. The Nusselt number on the outer wall in the turn is intensified and slightly shifted to the trailing wall side. After the turn, the high heat transfer area is divided into two parts on the outer wall. On the pressure side in the straight pass, the streak pattern appears both in the Nusselt number and the wall shear stress. In the instantaneous field (figures not shown), the streak pattern was clearly observed on the pressure surface of the whole straight pass, and, except the location in front of the sharp turn, it disappeared after the time averaging. One possible explanation of the streak pattern in the time-averaged field is that the large flow structure formed around the sharp turn interacted with the streak and made the streak persistent in space. However, further investigation is needed on this streak pattern.

For the higher Ro_* of Fig. 5 ($Ro_* = 2$), the reverse flow area recognized by the negative wall shear stress becomes larger at the turn entrance on the leading wall following the suction surface of the first straight pass. The streak pattern appears even in the turn (see the turn A of the trailing wall in Fig. 5(a)). In the straight pass, alternating pattern appears on the suction surfaces.

Fig. 6 shows the time-averaged velocity vectors $(\bar{u}, \bar{v})$ and the isocontours of the time-averaged normal velocity component to the cross-section, $\bar{w}$, and temperature, $\bar{\theta}$, for the stationary condition. In the figure, the values at five different z locations in and around the turn A are shown: from top to bottom $z = 18.9$, 18.0, 16.9, 15.0, and 13.0 (note that $z = 19.0$ and 17.0 correspond to the outer end wall and the tip of the inner wall, respectively). It should be noted that the scale of the velocity vectors for $z = 15.0$ and 13.0 are different from the rest in order to magnify the weaker secondary flow at these two locations. Even at $2D$ upstream of the turn

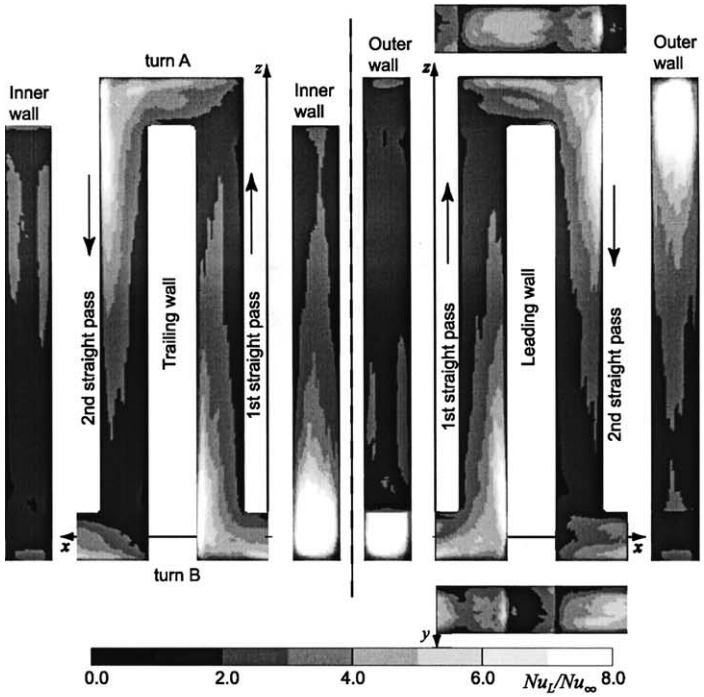

(a) Nusselt number

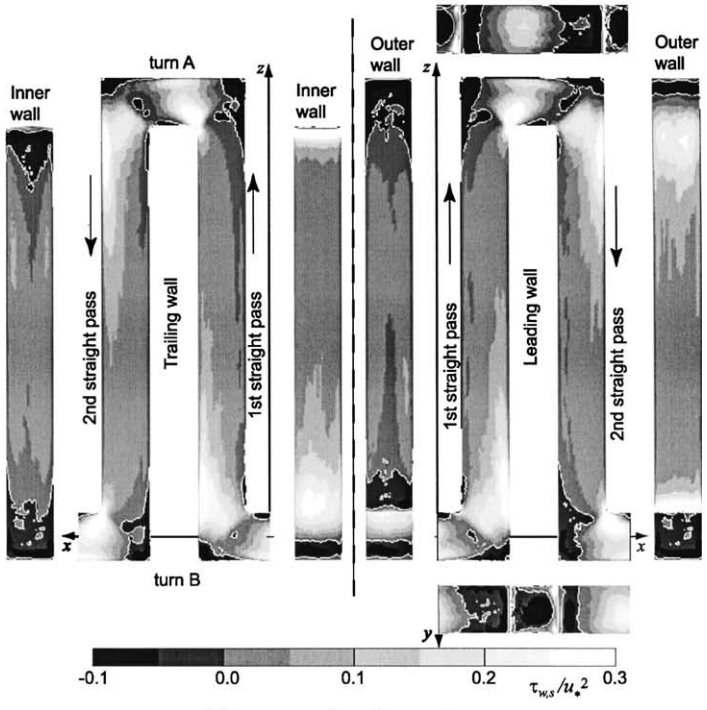

(b) streamwise shear stress

Fig. 3. Time-averaged profiles of Nusselt number and streamwise component of wall shear stress on the walls ($Re_* = 700$, $Re_m = 4099$, and $Ro_* = 0$).

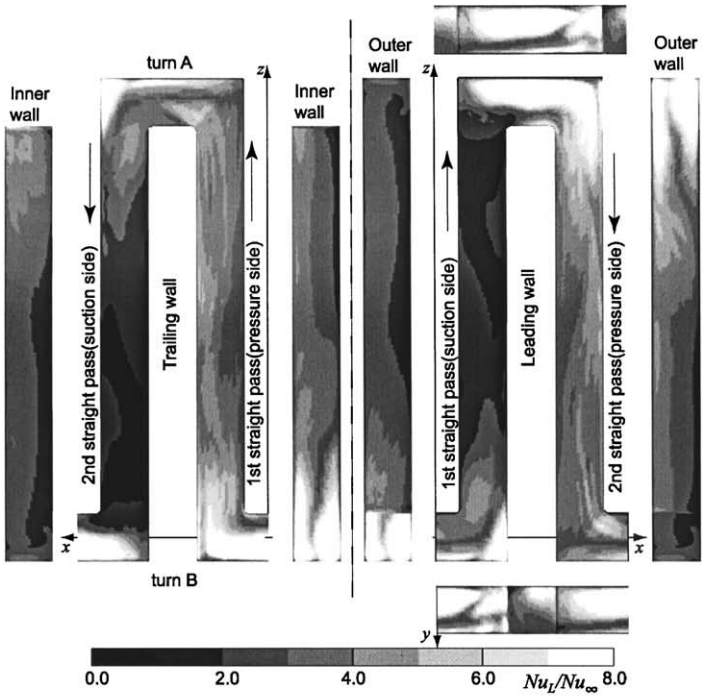

(a) Nusselt number

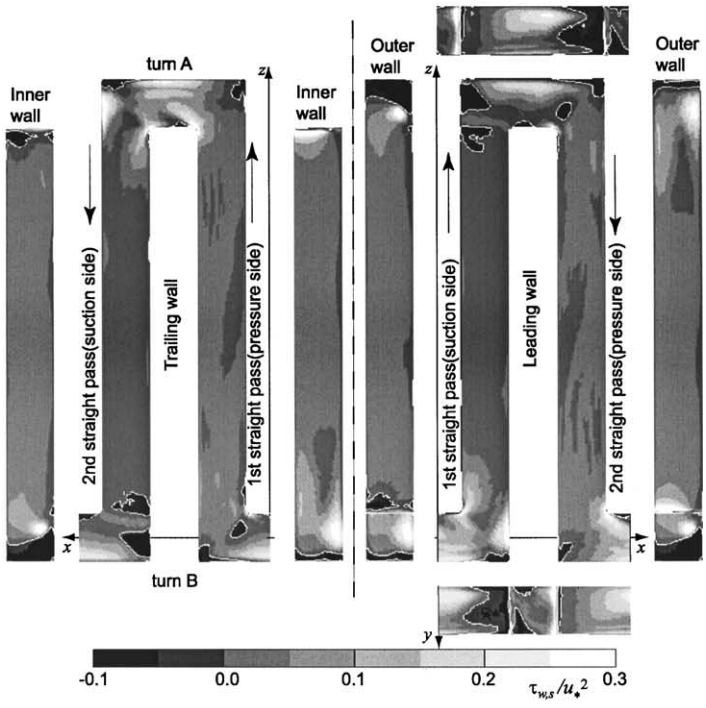

(b) streamwise shear stress

Fig. 4. Time-averaged profiles of Nusselt number and streamwise component of wall shear stress on the walls ($Re_* = 1000$, $Re_m = 4028$, $Ro_* = 1$, and $Ro_m = 0.99$).

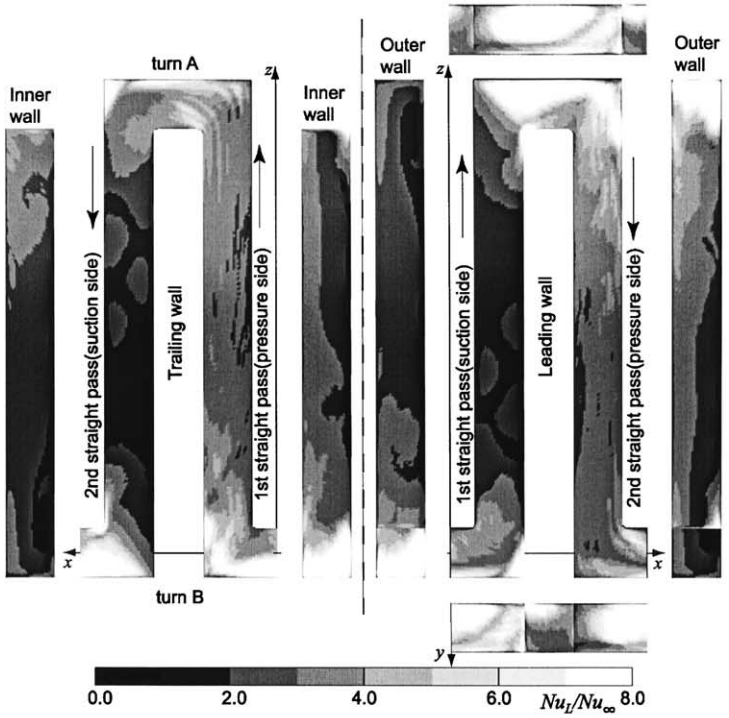

(a) Nusselt number

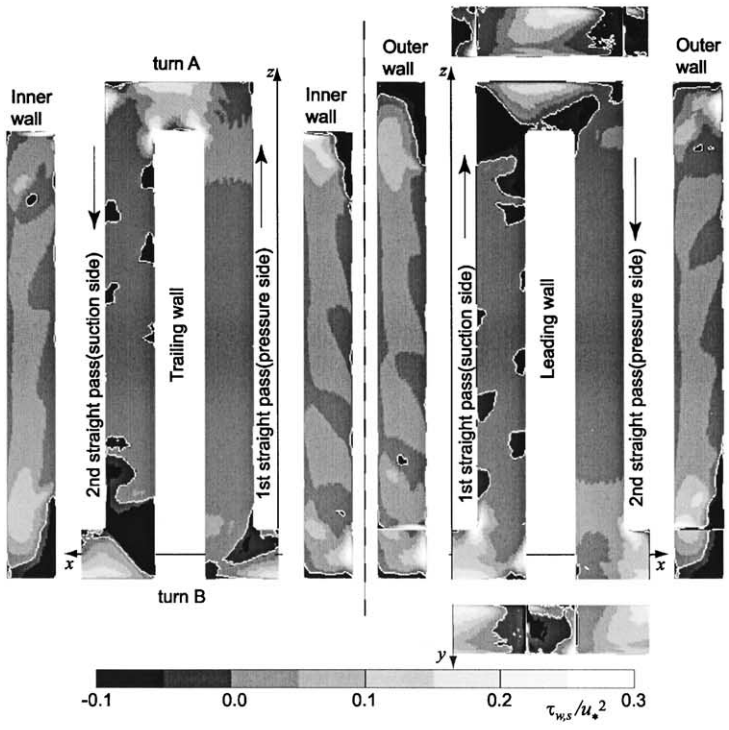

(b) Streamwise Shear Stress

Fig. 5. Time-averaged profiles of Nusselt number and streamwise component of wall shear stress on the walls ($Re_* = 1500$, $Re_m = 3926$, $Ro_* = 2$, and $Ro_m = 3.06$).

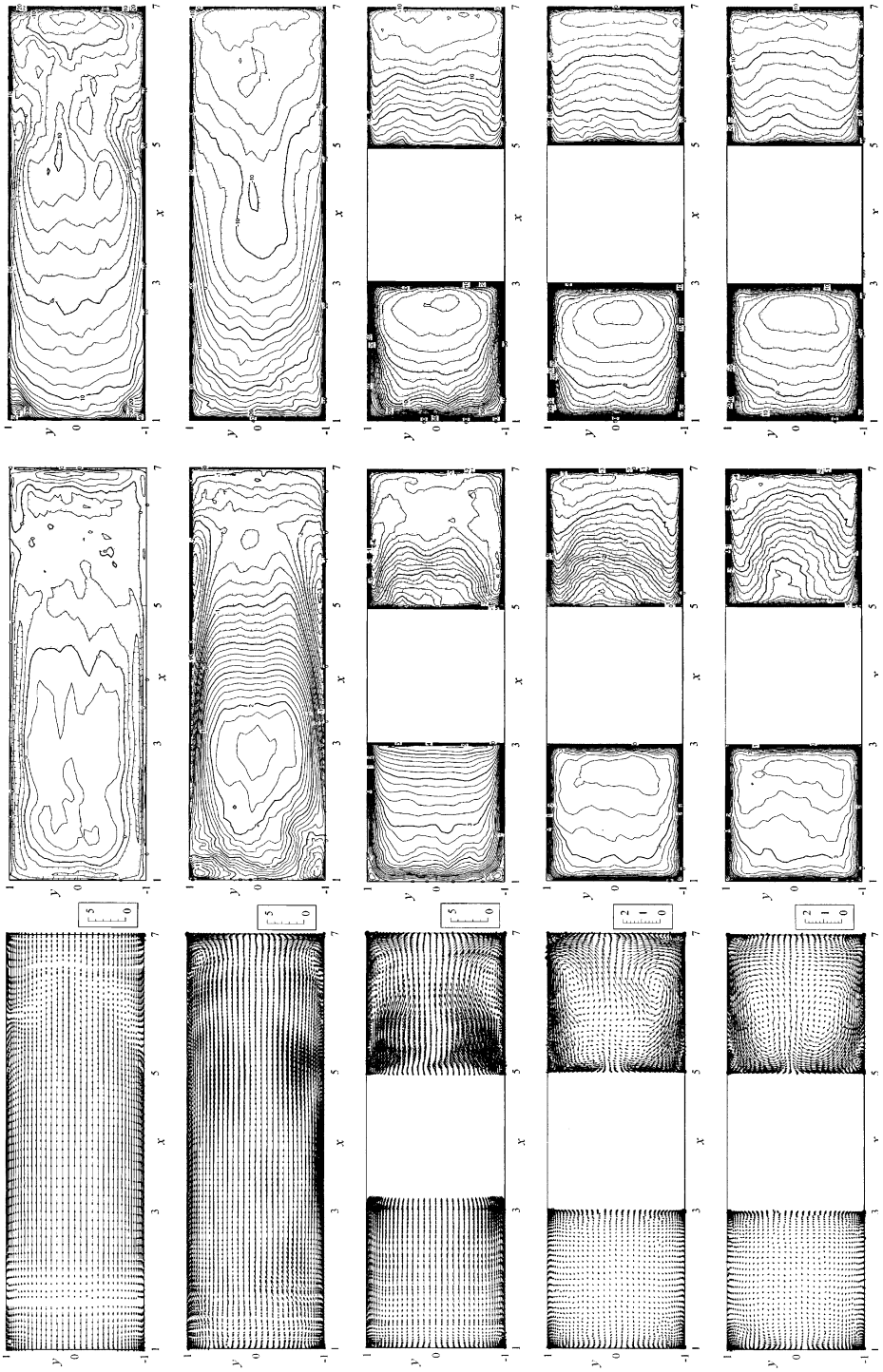

Fig. 6. Time-averaged velocity and temperature profiles in x–y planes for $Ro_* = 0$ (left, middle, and right figures are for velocity vectors $(\bar{u}, \bar{v})$, normal velocity component $\bar{w}$, and temperature $\bar{\theta}$, respectively. From top to bottom, $z = 18.9$, 18.0, 16.9, 15.0, and 13.0).

($1 < x < 3$ of the bottom figures), both $\bar{w}$ and $\bar{\theta}$ show the peak shifted to the inner wall and this indicates the remaining influence of the previous turn. At the entrance of the turn ($1 < x < 3$ of the third figures from top), the

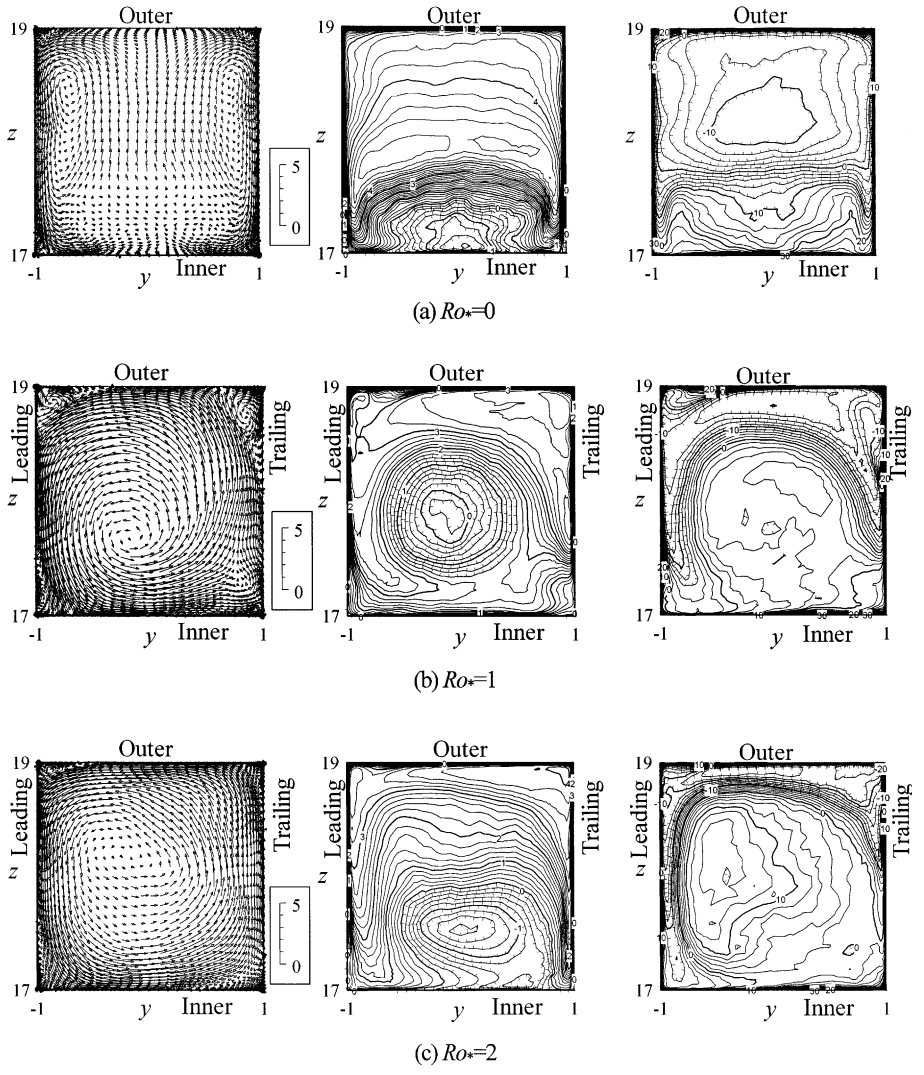

Fig. 7. Time-averaged velocity and temperature profiles in y–z mid-plane of turn A ($x = 4.0$) (left, middle, and right figures are for velocity vectors $(\bar{v}, \bar{w})$, normal velocity component $\bar{u}$, and temperature $\bar{\theta}$, respectively).

flow is accelerated to the inner wall side, and the high streamwise velocity region is shifted very close to the inner wall, although the temperature profile does not change much at the same location. This dissimilarity between $\bar{w}$ and $\bar{\theta}$ is the reason for the high wall shear stress near the inner wall corner without the heat transfer augmentation seen in Fig. 3. In the turn, the profile of $\bar{w}$ and $\bar{\theta}$ differs, and, after the turn, both the high streamwise velocity and low temperature regions are shifted to the outer wall. In the second straight pass, the convex profile of $\bar{w}$ on the inner wall side is due to the flow separation after the turn.

Fig. 7 shows the time-averaged velocity vectors $(\bar{v}, \bar{w})$ and the isocontours of the time-averaged streamwise velocity component, $\bar{u}$, and temperature, $\bar{\theta}$, in the y–z mid-plane of the turn A ($x = 4.0$). For $Ro_* = 0$ (Fig. 7(a)), the symmetric profile with respect to $y = 0$ is established. The flow separation is observed near the inner wall as a reverse flow region.

When the channel rotates (Fig. 8 for $Ro_* = 1$), in the first straight pass the Coriolis induced flow develops but still the previous turn effect remains. Therefore, the symmetric Coriolis induced secondary flow with respect to $x = 2$ cannot be seen. The profiles of $\bar{w}$ and $\bar{\theta}$ are already different to each other in the first straight pass. At the entrance of the turn ($1 < x < 3$ of the third figures from top), the peak of $\bar{w}$ is shifted to the trailing wall (the pressure side) and the flow acceleration to the inner wall is more intensified near the trailing wall. The high streamwise momentum impinges on the outer end wall

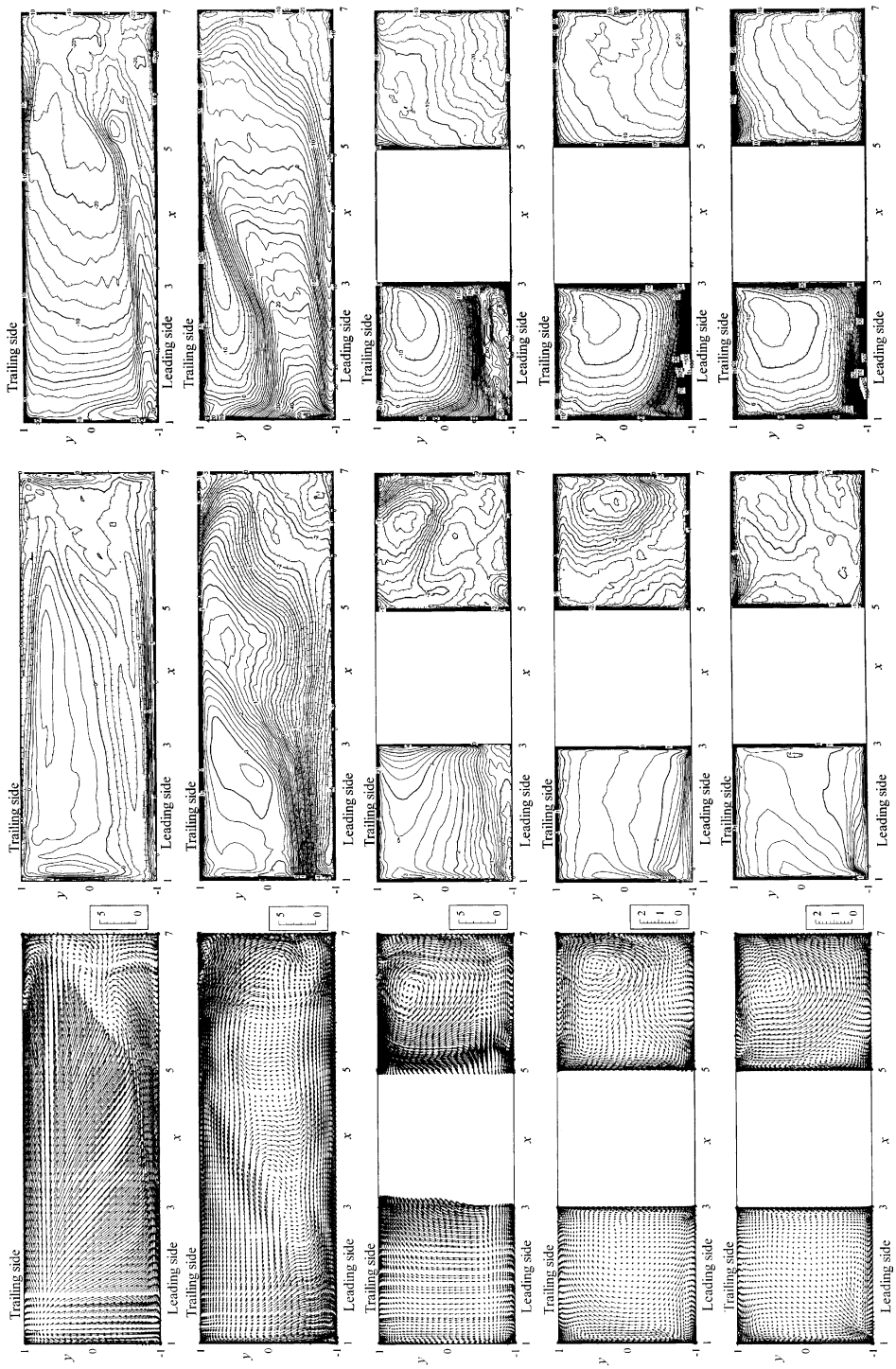

Fig. 8. Time-averaged velocity and temperature profiles in x–y planes for $Ro_* = 1$ (left, middle, and right figures are for velocity vectors $(\bar{u}, \bar{v})$, normal velocity component $\bar{w}$, and temperature $\bar{\theta}$, respectively. From top to bottom, $z = 18.9$, 18.0, 16.9, 15.0, and 13.0).

at the shifted location toward the trailing wall (see the top figures). In the turn, the flow structure becomes very complicated. The impinged flow downwashes the outer end wall from upper left to lower right direction. In the y–z mid-plane of the turn (Fig. 7(b)), the high momentum flow on the trailing side induces a dominating

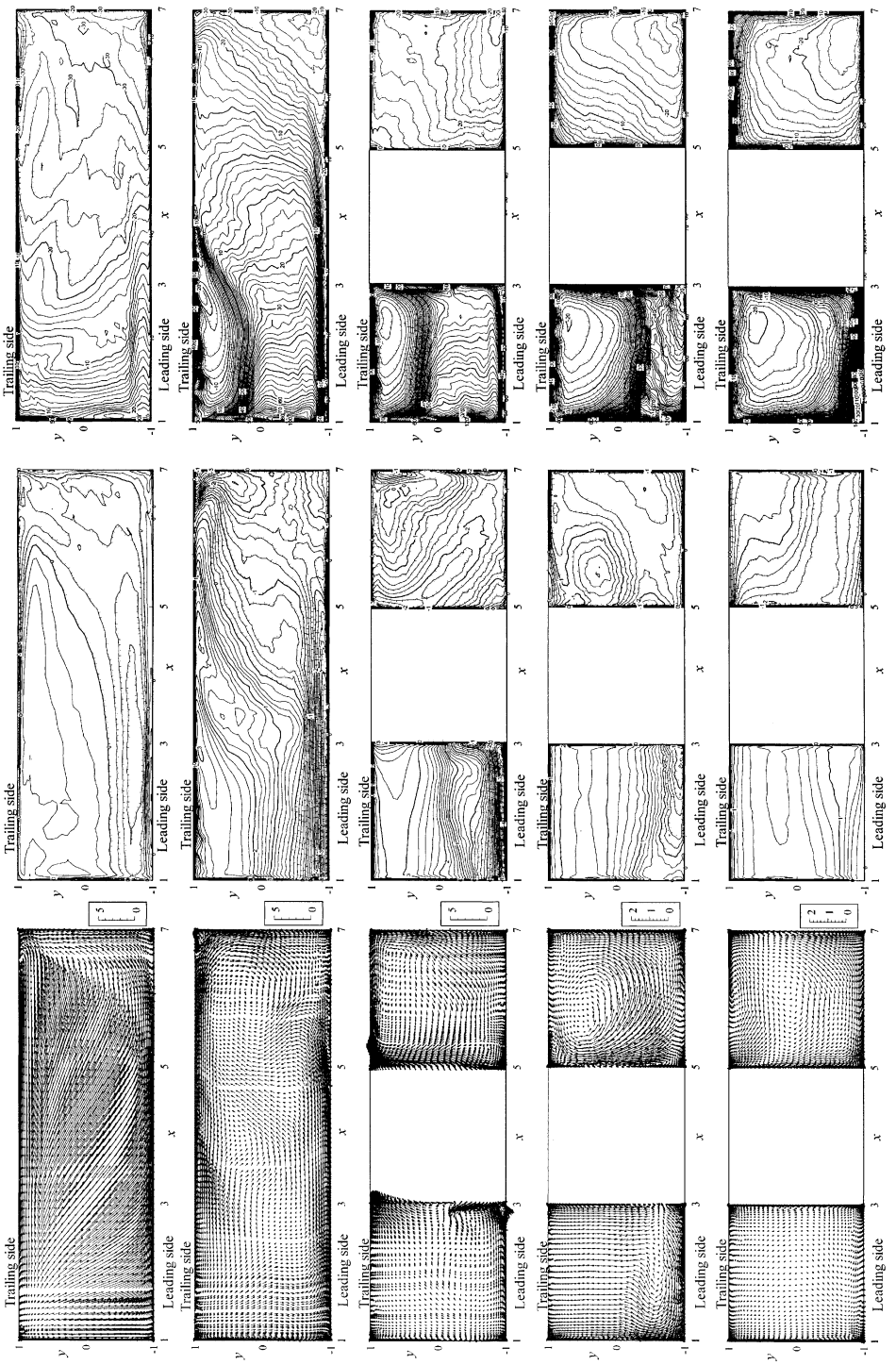

Fig. 9. Time-averaged velocity and temperature profiles in x–y planes for $Ro_* = 2$ (left, middle, and right figures are for velocity vectors $(\bar{u}, \bar{v})$, normal velocity component $\bar{w}$, and temperature $\bar{\theta}$, respectively. From top to bottom, $z = 18.9$, 18.0, 16.9, 15.0, and 13.0).

vortex which rotates in the counter-clockwise direction in the figure. Due to this strong vortex, the high momentum and low temperature fluid on the trailing side is transported to the leading side. At this y–z mid-plane, the reverse flow which located on the inner wall in the stationary condition (Fig. 7(a) center) shifts its location

to the central region due to the strong vortex (Fig. 7(b) center). After the turn, the strong vortex dominates at the turn outlet and at $z = 15.0$, but then the Coriolis force reverses the rotating direction of the vortex at $z = 13.0$. The low temperature region appears near the leading-outer corner, although the $\bar{w}$ shows a different complicated profile from that of $\bar{\theta}$.

For the higher rotation speed of $Ro_* = 2$ (Fig. 9), in the first straight pass, the profile of $\bar{w}$ becomes uniform in the x direction. This phenomenon is called the Taylor–Proudman effect [34] due to the balance between the pressure gradient and the Coriolis force which does not have a component in the x direction. In the y–z midplane of Fig. 7(c), judging from the reduced size of the corner vortices, the strong vortex is more intensified in the near-wall region, and the high momentum and low temperature fluid is further transported to the leading wall as compared to $Ro_* = 1$ of Fig. 7(b). In the second straight pass of Fig. 9, due to the high rotating speed, the recovery of the $\bar{w}$ profile from that disturbed by the sharp turn to that uniform in the x direction seems quicker as compared to Fig. 8 of $Ro_* = 1$.

Fig. 10 shows the duct-axial variation of the area-averaged Nusselt number, Nu_{area}. In order to show the approximate tendency, the area average was taken with the pitch of D in the duct-axial direction for each wall in addition to the transverse average. The inner and outer wall results are shown in Fig. 10(a), and the leading and trailing wall results are in Fig. 10(b). The thin, middle, and thick line widths correspond to $Ro_* = 0$, 1, and 2, respectively. As seen in Fig. 10(a), the outer wall gives the two peaks in the turn, and the channel rotation makes the two peaks higher. For $Ro_* = 2$, the levels of the two peaks become comparable to each other. Around the turn, the Nusselt number on the inner wall is also increased by the rotation, but the values are lower than those on the outer wall. The trailing and leading walls in Fig. 10(b) give the increased and decreased values in the first pass, respectively. The situation is reversed in the second straight pass, because the pressure and suction sides are changed depending on the radial flow direction. As was seen in Figs. 4 and 5, the rotation increases the Nusselt number on the leading wall in the turn A, and for $Ro_* = 2$ the Nusselt number on the leading wall becomes much higher than that on the trailing wall. In the straight pass, the heat transfer suppression on the suction surface is less intensive than the heat transfer augmentation on the pressure surface. This tendency is also supported by the experimental results [10,11,16].

The section-averaged Nusselt number is shown in Fig. 11. In the section average, the flow passage was divided into four sections: the turn B, the first straight pass, the turn A, and the second straight pass. The turn and straight sections were divided at the z location of the inner-wall tip: for the turn A at $z = 17.0$. In the stationary condition, the heat transfer of the turn is higher than that of the straight pass except the inner wall. The heat transfer enhancement caused by the rotation is also higher in the turn than in the straight pass. As seen in Fig. 5(a) and Fig. 10, for $Ro_* = 2$, the leading wall shows the maximum section-averaged value among the four walls. It should be noted again that, in the turn B, the inner and outer walls refers to the opposite sides, because the term "inner and outer" of this study was decided at the turn A location.

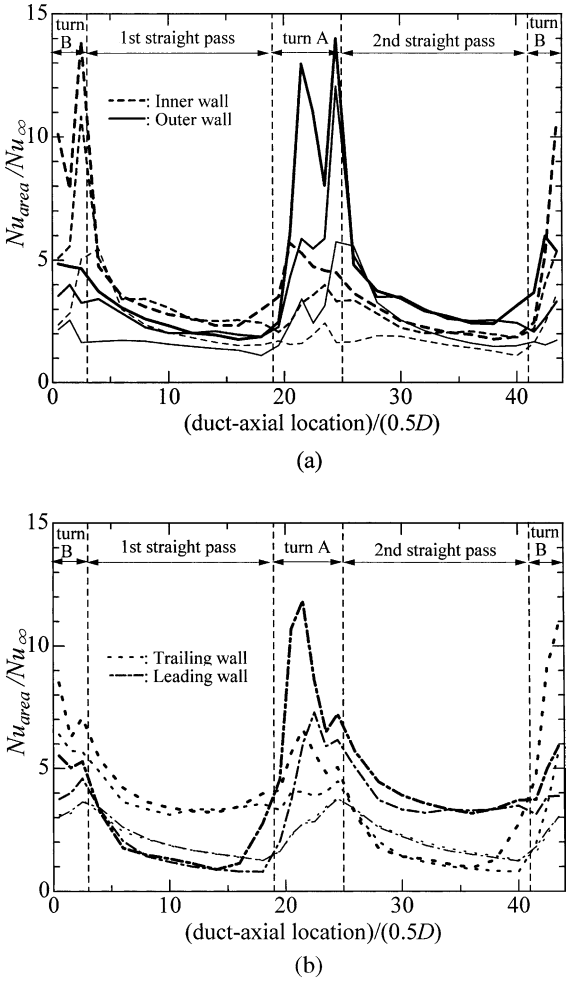

Fig. 10. Area-averaged Nusselt number variation in the duct-axial direction (area average was performed in transverse and duct-axial directions with duct-axial pitch of D; thin, middle, and thick lines are for $Ro_* = 0$, 1, and 2, respectively). (a) Inner and outer walls, (b) Leading and trailing walls.

Fig. 12 shows the Colburn's j factor and the friction factor, f. The j and f factors are normalized by using j_∞ calculated from Nu_∞ in Eq. (11) and f_{B} in the following Blasius equation:

$$f_{\mathrm{B}} = 0.079 Re_{\mathrm{m}}^{-0.25}. \tag{12}$$

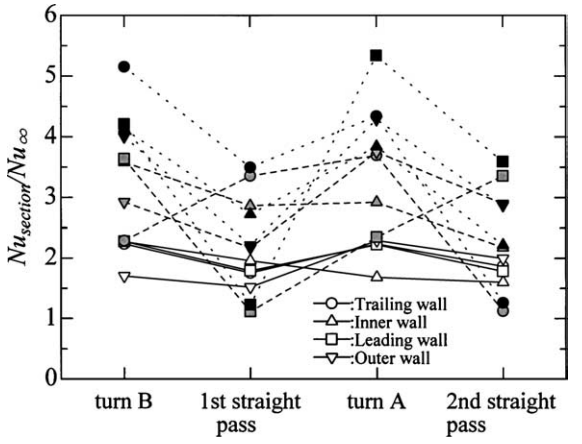

Fig. 11. Section-averaged Nusselt number variation (open, gray, and filled symbols are for $Ro_* = 0$, 1, and 2, respectively).

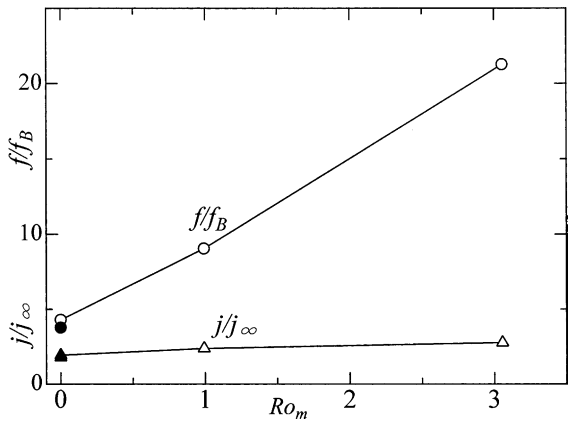

Fig. 12. Effect of rotation on f and j factors. (Open and filled symbols are for the numerical and experimental results, respectively. The f and j factors of the experimental results for $Re_m = 5000$ are from [3,2], respectively.).

The same results are summarized in Table 1 in order to show the increase percentage due to the channel rotation. In the figure, the experimental results [2,3] for $Ro_m = 0$ and $Re_m = 5000$ are also shown with the filled symbols for comparison. Considering that in the experiment only one turn existed and the spatial resolution of the temperature measurement was limited, the agreement between the experimental and numerical results is satisfactory. The f factor is sensitive to the introduction of the channel rotation and shows about 400% increase for $Ro_* = 2$ as compared to the stationary case; on the contrary, the j factor is relatively insensitive to the channel rotation and shows only about 40% increase for $Ro_* = 2$ as compared to the stationary case.

4. Conclusions

The large eddy simulation of the two-pass square channel with the 180° sharp turns was performed for both the stationary and rotating conditions. From the numerical results the following conclusions were drawn.

In the stationary condition, the heat transfer in and after the turn was increased. The characteristic flow behaviors in the sharp turn were the flow impingement onto the outer wall, the flow separation and reattachment on the inner wall, and the unsteady recirculation around the outer corners. The interesting situation was observed at the second outer corner where the high heat transfer region was produced by the reverse flow. The similarity between the streamwise velocity and the temperature was preserved before entering the turn, although in and after the turn it disappeared.

When the channel was rotated, the Coriolis force further complicated the flow and heat transfer distributions. In the turn, the trailing/leading wall located between the upstream suction to downstream pressure surfaces gave the higher heat transfer than the opposite wall. This high heat transfer was induced by the strong vortex in the turn that transported the high streamwise momentum and low temperature fluid from the pressure side to the suction side. For the highest rotation number, the Nusselt number level of this trailing/leading wall became comparable to that of the outer wall. In the rotating condition, the similarity between the streamwise velocity and the temperature was not observed even before the turn entrance.

The friction factor was very sensitive to the channel rotation, and for $Ro_* = 2$ it showed about 400% increase as compared to the stationary case. On the contrary, the channel averaged Nusselt number was relatively insensitive to the channel rotation, and it showed only about 40% higher value than that of the stationary case.

References

[1] J.-C. Han, Recent studies in turbine blade cooling, in: CD-ROM Proc. of the 9th Int. Symp. on Transport Phenomena and Dynamics of Rotating Machinery, Honolulu, Hawaii, US, Invited Lecture, 2002, pp. 1–16.

[2] A. Murata, S. Mochizuki, M. Fukunaga, Detailed measurement of local heat transfer in a square-cross-section duct with a sharp 180° turn, in: Heat Transfer 1994, Proc. of Int. Heat Transfer Conf., Brighton, G.B., vol. 4, 1994, pp. 291–296.

[3] S. Mochizuki, A. Murata, M. Fukunaga, Effects of rib arrangements on pressure drop and heat transfer in a rib-roughened channel with a sharp 180° turn, Trans. ASME, J. Turbomach. 119 (1997) 610–616.

[4] P.R. Chandra, J.C. Han, S.C. Lau, Effect of rib angle on local heat/mass transfer distribution in a two-pass rib-roughened channel, Trans. ASME, J. Turbomach. 110 (1988) 233–241.

[5] M. Hirota, H. Fujita, A. Syuhada, S. Araki, T. Yoshida, T. Tanaka, Heat/mass transfer characteristics in two-pass smooth channels with a sharp 180-deg turn, Int. J. Heat Mass Transfer 42 (1999) 3757–3770.
[6] S.V. Ekkad, J.C. Han, Detailed heat transfer distributions in two-pass square channels with rib turbulators, Int. J. Heat Mass Transfer 40 (11) (1997) 2525–2537.
[7] T.M. Liou, C.C. Chen, T.W. Tsai, Liquid crystal measurements of heat transfer in a 180° sharp turning duct with different divider thicknesses, in: CD-ROM Proc. of the 8th Int. Symp. on Flow Visualization, Sorrento, Italy, vol. 71, 1998, pp. 1–9.
[8] T. Astarita, G. Cardone, Thermofluidynamic analysis of the flow in a sharp 180° turn channel, Exp. Thermal Fluid Sci. 20 (2000) 188–200.
[9] S.Y. Son, K.D. Kihm, J.-C. Han, PIV flow measurements for heat transfer characterization in two-pass square channels with smooth and 90° ribbed walls, Int. J. Heat Mass Transfer 45 (2002) 4809–4822.
[10] J.-C. Han, Y.-M. Zhang, K. Kalkuehler, Uneven wall temperature effect on local heat transfer in a rotating two-pass square channel with smooth walls, Trans. ASME, J. Heat Transfer 115 (1993) 912–920.
[11] J.H. Wagner, B.V. Johnson, F.C. Kopper, Heat transfer in rotating serpentine passages with smooth walls, Trans. ASME, J. Turbomach. 113 (1991) 321–330.
[12] S. Mochizuki, J. Takamura, S. Yamawaki, W.-J. Yang, Heat transfer in serpentine flow passages with rotation, Trans. ASME, J. Turbomach. 116 (1994) 133–140.
[13] J.A. Parsons, J.-C. Han, Y.-M. Zhang, Effect of model orientation and wall heating condition on local heat transfer in a rotating two-pass square channel with rib turbulators, Int. J. Heat Mass Transfer 38 (7) (1995) 1151–1159.
[14] B.V. Johnson, J.H. Wagner, G.D. Steuber, F.C. Yeh, Heat transfer in rotating serpentine passages with trips skewed to the flow, Trans. ASME, J. Turbomach. 116 (1994) 113–123.
[15] S. Mochizuki, M. Beier, A. Murata, T. Okamura, Y. Hashidate, Detailed measurement of convective heat transfer in rotating two-pass rib-roughened coolant channels, ASME Paper, 96-TA-6, 1996.
[16] T.-M. Liou, C.-C. Chen, M.-Y. Chen, TLCT and LDV measurements of heat transfer and fluid flow in a rotating sharp turning duct, Int. J. Heat Mass Transfer 44 (2001) 1777–1787.
[17] B. Banhoff, U. Tomm, B.V. Johnson, I. Jennions, Heat transfer predictions for rotating U-shaped coolant channels with skewed ribs and with smooth walls, ASME Paper, 97-GT-162, 1997.
[18] Y.-L. Lin, T.I-P. Shih, M.A. Stephens, M.K. Chyu, A numerical study of flow and heat transfer in a smooth and ribbed U-duct with and without rotation, Trans. ASME, J. Heat Transfer 123 (2001) 219–232.
[19] A. Huser, S. Biringen, Direct numerical simulation of turbulent flow in a square duct, J. Fluid Mech. 257 (1993) 65–95.
[20] S. Gavrilakis, Numerical simulation of low Reynolds number turbulent flow through a straight square duct, J. Fluid Mech. 244 (1992) 101–129.
[21] R.K. Madabhushi, S.P. Vanka, Large eddy simulation of turbulence-driven secondary flow in a square duct, Phys. Fluids A3 (11) (1991) 2734–2745.
[22] A. Murata, S. Mochizuki, Effect of cross-sectional aspect ratio on turbulent heat transfer in an orthogonally rotating rectangular smooth duct, Int. J. Heat Mass Transfer 42 (1999) 3803–3814.
[23] J. Pallares, L. Davidson, Large eddy simulations of turbulent flow in a rotating square duct, Phys. Fluids 12 (11) (2000) 2878–2894.
[24] A. Murata, S. Mochizuki, Large eddy simulation of turbulent heat transfer in an orthogonally rotating square duct with angled rib turbulators, Trans. ASME, J. Heat Transfer 123 (2001) 858–867.
[25] A. Murata, S. Mochizuki, Effect of centrifugal buoyancy on turbulent heat transfer in an orthogonally rotating square duct with transverse or angled rib turbulators, Int. J. Heat Mass Transfer 44 (2001) 2739–2750.
[26] S.V. Patankar, C.H. Liu, E.M. Sparrow, Fully developed flow and heat transfer in ducts having streamwise-periodic variations of cross-sectional area, Trans. ASME, J. Heat Transfer 99 (1977) 180–186.
[27] T. Kajishima, T. Ohta, K. Okazaki, Y. Miyake, High-order finite-difference method for incompressible flows using collocated grid system, JSME Int. J. Ser. B 41 (4) (1998) 830–839.
[28] C. Meneveau, T.S. Lund, W.H. Cabot, A Lagrangian dynamic subgrid-scale model of turbulence, J. Fluid Mech. 319 (1996) 353–385.
[29] P. Moin, K. Squires, W. Cabot, S. Lee, A dynamic subgrid-scale model for compressible turbulence and scalar transport, Phys. Fluids A3 (11) (1991) 2746–2757.
[30] F.H. Harlow, J.E. Welch, Numerical calculation of time-dependent viscous incompressible flow of fluid with free surface, Phys. Fluids 8 (12) (1965) 2182–2189.
[31] J. Kim, P. Moin, Application of a fractional-step method to incompressible Navier–Stokes equations, J. Comp. Phys. 59 (1985) 308–323.
[32] Y. Zang, R.L. Street, J.R. Koseff, A non-staggered grid, fractional step method for time-dependent incompressible Navier–Stokes equations in curvilinear coordinates, J. Comp. Phys. 114 (1994) 18–33.
[33] W.M. Kays, M.E. Crawford, Convective Heat and Mass Transfer, 3rd ed., McGraw-Hill Inc, New York, 1993, p. 316.
[34] G.K. Batchelor, An Introduction to Fluid Dynamics, Cambridge University Press, 1967, pp. 555–559.